# Zincate-Blocking Functionalized Polysulfone Separators for Secondary Zn-MnO₂ Batteries

*Igor V. Kolesnichenko,[1] David J. Arnot,[1] Matthew B. Lim,[2] Gautam G. Yadav,[3] Michael Nyce,[4] Jinchao Huang,[3] Sanjoy Banerjee,[3,4] Timothy N. Lambert[1]* *

[1] Department of Photovoltaics and Materials Technology, Sandia National Laboratories, Albuquerque, NM 87185-0734, USA

[2] Department of Energy Storage Technology and Systems, Sandia National Laboratories, Albuquerque, New Mexico, United States, 87185

[3] Urban Electric Power, 401 N Middletown Rd, Pearl River, NY 10965, USA

[4] Department of Chemical Engineering, The CUNY Energy Institute at the City College of New York, Steinman Hall, 140th Street and 160 Convent Avenue, Room 316, New York, 10031, New York, USA

**Keywords:** Zinc batteries; selective separators; functionalized polysulfone; zincate blocking; crossover; cycle life

## Abstract

Alkaline zinc-manganese dioxide (Zn–MnO₂) batteries are well suited for grid storage applications due to their inherently safe, aqueous electrolyte and established materials supply chain, resulting in low production costs.  With recent advances in the development of Cu/Bi-stabilized birnessite cathodes capable of the full 2-electron capacity equivalent of MnO₂ (617 mAh/g), there is a need for selective separators that prevent zincate $(Zn(OH)_4)^{2-}$ transport from the anode to the cathode during cycling, as this electrode system fails in the presence of dissolved zinc. Herein, we present the synthesis of N-butylimidazolium-functionalized polysulfone (NBI-PSU)-based separators and evaluate their ability to selectively transport hydroxide over zincate. We then examine the impact on the cycling of high depth of discharge Zn/(Cu/Bi–MnO₂) batteries when inserted in between the cathode and anode.  Initially, we establish our membrane's selectivity by performing zincate and hydroxide diffusion tests, showing a marked improvement in zincate-blocking ($D_{Zn}$ (cm²/min): $0.17 \pm 0.04 *10^{-6}$ for 50-PSU, our most selective separator vs. $2.0 \pm 0.8$

$*10^{-6}$ for cellophane 350P00 and $5.7 \pm 0.8 *10^{-6}$ for Celgard 3501), while maintaining similar crossover rates for hydroxide ($D_{OH}$ (cm$^2$/min): $9.4 \pm 0.1 *10^{-6}$ for 50-PSU vs. $17 \pm 0.5 *10^{-6}$ for cellophane 350P00 and $6.7 \pm 0.6 *10^{-6}$ for Celgard 3501). We then implement them into cells and observe an improvement in cycle life over control cells containing only the commercial separators (cell lifetime extended from 21 to 79 cycles).

## Introduction

As society transitions away from fossil fuels, clean and renewable power sources such as wind and solar energy are increasingly being integrated into the electrical grid. However, the intermittent nature of such sources highlights the need for energy storage systems that can collect and/or release electricity when renewable output mismatches transmission capacity or demand. Rechargeable battery-based systems for grid storage are gaining popularity due to their ease of manufacture, scalability to desired capacities, and modularity.

To be successful, a grid-integrated battery system should have high energy density, long cycle life (> 5,000 cycles), low production cost (< \$100 kWh$^{-1}$), and minimal hazards.[1] Alkaline zinc-manganese dioxide (Zn–MnO$_2$) batteries, which have a Zn anode, MnO$_2$ cathode, and aqueous KOH electrolyte, are a promising candidate if sufficient rechargeability can be achieved.[2] First patented in 1960 and now ubiquitous as disposable batteries in everyday electronics, primary Zn–MnO$_2$ batteries have energy densities of up to 400 Wh L$^{-1}$ or 150 Wh kg$^{-1}$, rivaling lithium-ion batteries, along with abundant raw materials and a long-established supply chain that puts their cost as low as \$20 kWh$^{-1}$.[3-5] Furthermore, Zn–MnO$_2$ batteries have a lower environmental impact than other types of batteries, having a non-flammable aqueous electrolyte and even EPA certification for landfill disposal in the United States.[6]

The biggest challenge to implementing alkaline Zn–MnO$_2$ batteries in the grid is their historically poor rechargeability due to irreversible processes in each electrode during discharge. In theory, both electrode materials can undergo two-electron redox processes to impart high specific capacities of 820 mAh g$^{-1}$ for Zn and 617 mAh g$^{-1}$ for MnO$_2$. For MnO$_2$, the first- and second-electron reduction reactions occur by distinct mechanisms, the former through proton

intercalation and the latter, through dissolution-precipitation. However, conventional primary cells cannot deliver much beyond the first-electron capacity of $MnO_2$ (308 mAh g$^{-1}$) due to the formation of insulating, electrochemically inactive spinel compounds in the cathode during the second-electron process. These compounds are hausmannite ($Mn_3O_4$) and hetaerolite ($ZnMn_2O_4$), the latter of which forms in the presence of zincate $(Zn(OH)_4)^{2-}$, which is the soluble discharge product of the Zn anode in alkaline electrolyte and can pass through the separator to the cathode.[7-9] If the system is repeatedly charged and discharged fully without significant modifications to the system or testing protocol, these inactive phases will continue to form and contribute to severe capacity fade within a few tens of cycles. The solubility of zincate is also detrimental to the anode capacity over repeated cycling, since it can lead to spatial redistribution of active material over the anode and effective loss of active material surface area.[10-13]

These problems can be partially mitigated by only accessing a small fraction of the theoretical capacity of each electrode during each cycle (e.g. $\leq 20\%$ of the first $MnO_2$ electron and $\leq 2.5\%$ of Zn capacity). This avoids spinel formation, prevents proton insertion from irreversibly expanding the crystal structure of $MnO_2$, and minimizes solubilization of Zn. Ingale et al.[14] showed that this limited depth of discharge (DOD) approach enabled over 1,000 cycles for prototype prismatic Zn–$MnO_2$ cells with minimal capacity loss, but at the obvious cost of energy density ($\leq 40$ Wh L$^{-1}$). Nevertheless, this technology has since been commercialized by startup company Urban Electric Power to 200–350 Ah cells that can be linked to form stationary battery systems with up to 16 kWh of usable energy.[15] Later, Yadav et al.[5] showed that the combination of $Bi_2O_3$, Cu, and carbon nanotubes with conventional $\gamma$-$MnO_2$ cathode material allowed it to deliver close to the full two-electron capacity for over 1,000 cycles at loadings as high as 60 wt. % $MnO_2$ (29 mAh cm$^{-2}$), albeit only in the absence of Zn. Unfortunately, when paired with Zn

anodes, the performance is much less impressive; even at a modest Zn utilization of 15%, the cells only deliver the full two-electron capacity equivalent of $MnO_2$ for ~80 cycles before fading and exhibit energy losses on the order of 20% in the first ten cycles due to side reactions of the cathode with zincate.[16] To achieve the ultimate goal of long cycle life for a Zn–$MnO_2$ system with high active material loadings and utilization, it is therefore imperative to develop low-cost separators that can effectively isolate the cathode from zincate.

The ideal separator will maintain good wettability and high ionic conductivity for hydroxide and alkali ions, while blocking or limiting zincate diffusion. While much research has been published on separators for lithium-ion batteries,[17-22] far less has been shown in the literature for alkaline zinc-based batteries. To date, the most commonly-used separator materials in batteries with zinc anodes have been unfunctionalized polymers like polyvinyl alcohol (PVA),[23-24] cellophane, and microporous polyolefins such as Celgard (polypropylene or polypropylene-coated polyethylene).[25-28] However, these materials on their own offer little to no transport selectivity towards specific ionic species.[29-30] Addition of a sheet composed of $Ca(OH)_2$ bound together by a small amount of Teflon and inserted between the anode and separator was shown by Huang and co-workers to serve as a zincate trap, forming an insoluble [$Ca(OH)_2 \cdot 2Zn(OH)_2 \cdot 2H_2O$] complex and suppressing the formation of spinel phases.[31] Yadav et al. then furthered this work by incorporating the calcium hydroxide interlayer into cells containing Bi/Cu-stabilized $MnO_2$ cathodes and observing over 900 cycles in the $2^{nd}$ electron regime of $MnO_2$.[16] Despite these promising results the $Ca(OH)_2$ interlayer proved ineffective from a practical standpoint due to its substantial thickness, which in turn diminished the cells' volumetric energy densities. While polymeric membranes have a number of drawbacks, such as varying degrees of hydrophobicity

and insulating properties, they are also versatile, offering a wide variety of backbones and easily tunable functionalization to include charges and/or chelating moieties.

One strategy is to incorporate charged functionalities on the polymer backbone of separator materials to improve their wettability, ionic conductivity, and perm-selectivity. For example, Dewi and co-workers showed a six-fold increase in capacity when using a synthesized cationic polysulfonium separator, as opposed to Celgard 5550 in an alkaline Zn–air battery.[32] However, the perm-selectivity of this separator for hydroxide was only observed at concentrations below 1 M KOH, and the capacity was still less than 100 mAh $g^{-1}$ for a full discharge – both impractically low for a commercial battery. Several commercial anion exchange ionomers have been coated on or impregnated into Zn or ZnO-based anodes for Zn–Ni and Zn–air systems.[33-36] Encapsulation of ZnO nanoparticles with carbon and ceramics has also been demonstrated.[37-38] While not strictly separators, they can similarly confine zincate ions near their point of origin to limit active material redistribution and possibly crossover, and have been demonstrated at higher KOH concentrations (4 M). Wu et al. treated Celgard 2320 membranes with concentrated sulfuric acid at 90°C to incorporate sulfonic acids on the polypropylene backbone, increasing its anionic conductivity by 132% in 32 wt. % KOH and improving power density from 20 mW $cm^{-2}$ to 38 mW $cm^{-2}$ when used in a Zn–air cell.[39] However, the separators were only tested in a primary system.

An alternate approach to bulk functionalized polymers is highly interwoven nanofibrous polymers, which can be infilled with additives to form size-dependent conductive pathways favoring transport of smaller hydroxide ions over larger zincate ions. Huang et al. demonstrated this by fabricating a separator composed of layers of graphene oxide and PVA to substantially improve energy densities of primary Zn–$MnO_2$ batteries.[40, 41] Unfortunately, the iterative nature of the membranes' construction as well as the limited improvement in cycle life of secondary cells

6

render this approach unviable on commercial scale. Alternatively, Lee and co-workers showed an electrospun polyetherimide (PEI) membrane impregnated with PVA[42] and subsequently a composite PVA/polyacrylic acid (PAA) nanofiber mat impregnated with a perfluorinated sulfonic acid-containing polymer (Nafion 521).[43] While both of these outperformed Celgard 3501 in alkaline Zn–air battery cycling experiments with 6 M KOH, capacity fade was still significant at deep DOD, falling from 645 to ~20 mAh g$^{-1}$ in the first five cycles.[42]

To investigate selective separators specifically for the alkaline Zn–MnO$_2$ system, Duay et al. evaluated a commercial sodium ion-conducting ceramic (NaSICON) membrane, which is 100% impervious to zincate. Under limited DOD conditions, cycle life was improved 122% over Celgard 3501 and Cellophane 350P00. However, the membrane ultimately proved to be too resistive to be practical.[44] The thick (0.5 mm), brittle and monolithic nature of NaSICON also complicated battery construction and reduced volumetric energy density.

Currently there are not many examples in the literature of synthesized separators, especially those stepping away from a polypropylene backbone (currently the most prevalent in commercial cells). A general increase in the variety of backbone and functionalization types to contrast with widely used commercial membranes would be helpful in guiding future enhancements in Zn–MnO$_2$ battery cycling research. In an effort to achieve this while working with a well-established, readily available, and easily modifiable subset of polymers, we chose to examine the effects of polysulfone functionalization on zincate blocking and battery cycle life. A cationic moiety was selected for incorporation as opposed to an anionic one due to the likelihood of better wetting and interactions with a highly alkaline (negatively charged) electrolyte, potentially allowing for more hydroxide crossover. Specifically, we examine blends of N-butylimidazolium-functionalized polysulfone with unmodified polysulfone to improve selectivity for hydroxide over zincate

transport and report our preliminary studies of use in secondary Zn–MnO$_2$ batteries.  To our knowledge, this is the first reported investigation and demonstration of performance improvement of polysulfone-based separators for alkaline Zn–MnO$_2$ systems.

## Results and Discussion

To examine the effect of degree of functionalization on the zincate transport properties of polysulfone, we used blends of functionalized and unaltered polymer.  By initially synthesizing a more highly functionalized polysulfone and then blending it in various percentages with the commercially available starting material, we aimed to mimic polymers functionalized to the corresponding specific degrees.   To achieve this, we first synthesized a chloromethylated polysulfone (CMPSU), adjusting reaction time and amounts of chloromethylating reagent used to achieve a degree of chloromethylation of nominally one per repeat unit of polymer – this was the key synthetic step in controlling the amount of functionalization.  Next, we reacted CMPSU with N-butylimidazole, leaving the polysulfone backbone appended with N-butylimidazolium at the established degree of functionalization of one (**Figure 1**).  After removing as much residual solvent as possible and characterizing the final product by NMR, the polymer was dissolved in *N,N*-dimethylformamide (DMF) at 5 wt. %. Separately, a 5 wt. % solution of unaltered polysulfone was also prepared in DMF and these solutions were blended in ratios of 3:1 and 1:1 to give overall degrees of functionalization of 25% and 50%, respectively.  Finally, 3 mL aliquots of these solutions, as well as the functionalized polymer alone to comprise the 100% analog, were casted and dried at 75°C to yield the finished membranes.
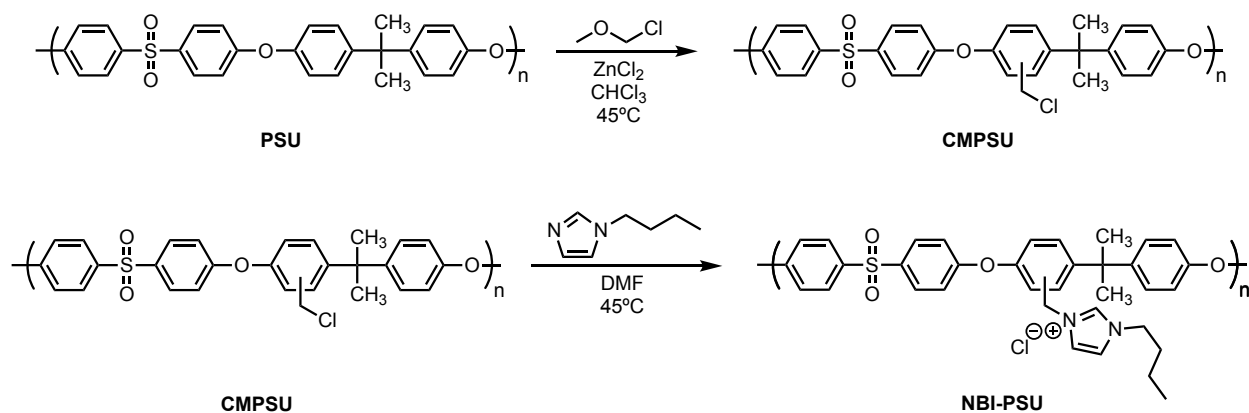
**Figure 1.** Synthesis of N-butylimidazolium-functionalized polysulfone (PSU).

Next, we characterized the physical and ion transport properties of the casted membranes and compared them to commercial battery separators (**Table 1**). The thickness of our PSU separators was 30 μm – within the same range as the commonly used commercial Cellophane 350P00 (24.4 μm) and Celgard 3501 (25 μm).[45-46] The structure of Celgard is porous polypropylene with an average pore size of 64 nm and porosity of 55%, while cellophane is a more hydrophilic regenerated cellulose film with few (if any) pores. A direct correlation in our synthesized and blended separators was found between the degree of functionalization (number of charged groups per repeat unit) and their chemical and physical properties. For example, polymer solutions with a high degree of functionalization resulted in separators that exhibited high water uptake, but also became more brittle and stiffer when dry. On the other hand, lower degrees of functionalization obtained by blending with unmodified polysulfone resulted in separators that were more hydrophobic, but mechanically stronger and easier to work with. Polymer membranes that were 100%, 50%, and 25% butylimidazolium-functionalized polysulfone (designated 100-PSU, 50-PSU, and 25-PSU, respectively) were chosen to be characterized, while the 50% functionalized membrane was further tested in rechargeable Zn–MnO$_2$ cells.

9

**Table 1. Properties of Commercial and Synthesized Separators**

| Separator | $D_{OH}$ (cm²/min) *10⁻⁶ | $D_{Zn}$ (cm²/min) *10⁻⁶ | Selectivity $R_s$ | Water Uptake (%) | Thickness (μm)[a] | Conductivity (mS/cm) | Functionalization (groups/repeat unit)[b] |
|---|---|---|---|---|---|---|---|
| Celgard 3501 | $6.7 \pm 0.6$ | $5.7 \pm 0.8$ | $1.2 \pm 0.2$ | $72 \pm 5$ | $25 \pm 1$ | $12 \pm 1.2$ | N/A[c] |
| Cellophane 350P00 | $17 \pm 0.5$ | $2.0 \pm 0.8$ | $8.5 \pm 3$ | $98 \pm 3$ | $25 \pm 1$ | $14 \pm 1.4$ | N/A[c] |
| 100-PSU | $15 \pm 0.2$ | $0.42 \pm 0.02$ | $36 \pm 2$ | $54 \pm 9$ | $30 \pm 5$ | $9.0 \pm 1.4$ | 0.98 |
| 50-PSU | $9.4 \pm 0.1$ | $0.17 \pm 0.04$ | $55 \pm 10$ | $26 \pm 8$ | $30 \pm 5$ | $7.2 \pm 1.9$ | 0.49 |
| 25-PSU | $2.5 \pm 0.1$ | $0.049 \pm 0.002$ | $51 \pm 3$ | $13 \pm 3$ | $30 \pm 5$ | $5.8 \pm 0.4$ | 0.25 |
| 0-PSU | $\leq 0.00005$[d] | N/A | N/A | $2.9 \pm 0.5$ | $30 \pm 5$ | $0.3 \pm 0.1$ | 0 |

[a]Measurements taken on dry membranes.
[b]Number of functional groups per repeat unit of polysulfone; measured using nuclear magnetic resonance integrations.
[c]Not Applicable
[d]Changes in pH for this measurement appeared to be due to electrode drift rather than consistent hydroxide diffusion.

The rate of ion transfer across each separator was determined using a two-chamber diffusion cell. Diffusion coefficients for hydroxide and zincate ions were calculated for each separator using equation 1,

$$D_x \; = \; \frac{V_D \tau}{At} \ln \left( \frac{C_F}{C_F - C_D} \right) \tag{1}$$

where $D_x$ is the diffusion coefficient for hydroxide or zincate ($D_{OH}$ or $D_{Zn}$, respectively), $V_D$ is the volume of the draw solution, $\tau$ is the separator thickness, $A$ is the cross-sectional area (1.17 cm²), $t$ is the elapsed experimental time, $C_F$ is the concentration in the feed solution, and $C_D$ is the concentration in the draw solution where concentration is measured. These diffusion coefficients are normalized to thickness and provide a simple metric to evaluate the ion transport properties of each separator. The hydroxide diffusion measurements used an 8.5 M KOH solution for the feed side of the cell and deionized water in the draw side of the cell. For the zincate diffusion measurements, both feed and draw solution consisted of 8.5 M KOH with 2.5 ppm Pb, 2.5 ppm Cd, and 5 ppm Bi, with the feed solution also containing 4 wt. % ZnO, prepared by dissolving ZnO. A pH meter was used to measure the hydroxide concentration over time and anodic stripping

voltammetry (ASV) was used to measure zincate concentration over time. ASV provides rapid zincate crossover determination in real time, at the lowest limit of detection, and can be done in highly alkaline electrolyte.[30]

For hydroxide diffusion experiments, the chambers were iteratively separated by each membrane and the pH was measured on the DI water-containing side as a function of time. As expected, increased functionalization and water uptake were associated with an increase in hydroxide diffusivity (**Table 1**, **Figure 2**). Adding more charged functional groups to the PSU separators was directly related to an increase in water uptake, which corresponded to a higher hydroxide diffusion coefficient. Comparison of the synthesized and commercial separators showed that they all exhibited hydroxide diffusion coefficients with the same order of magnitude, with the 100-PSU and 50-PSU variants being more permeable to hydroxide than the more hydrophobic Celgard ($D_{OH}$ = 15 ± 0.2 x $10^{-6}$, 9.4 ± 0.1 x $10^{-6}$, and 6.7 ± 0.6 *$10^{-6}$ cm$^2$ min$^{-1}$, respectively). The 25-PSU separator demonstrated a $D_{OH}$ of 2.5 ± 0.1 x $10^{-6}$ cm$^2$ min$^{-1}$, which is lower than the Celgard separator. This is expected because the low water uptake of 13 ± 3 % indicates that the separator is quite hydrophobic. Notably, the water uptake percentages of the 100-PSU and 50-PSU separators were 54 ± 9 % and 26 ± 8 %, respectively, which are also both lower than Celgard's water uptake of 72 ± 5 %. The higher $D_{OH}$ values, but lower water uptake of the functionalized PSU separators indicates that the functionalized polymers aided hydroxide transport. This conclusion is further supported by a comparison to cellophane. The water uptake of cellophane is 81% higher than 100-PSU, but the $D_{OH}$ of cellophane is only 13 % higher. The fact that our separators absorb less water while maintaining appreciable hydroxide permeability may actually be desirable for grid storage batteries that are designed to cycle for months or years, by reducing swelling and associated mechanical degradation.

11
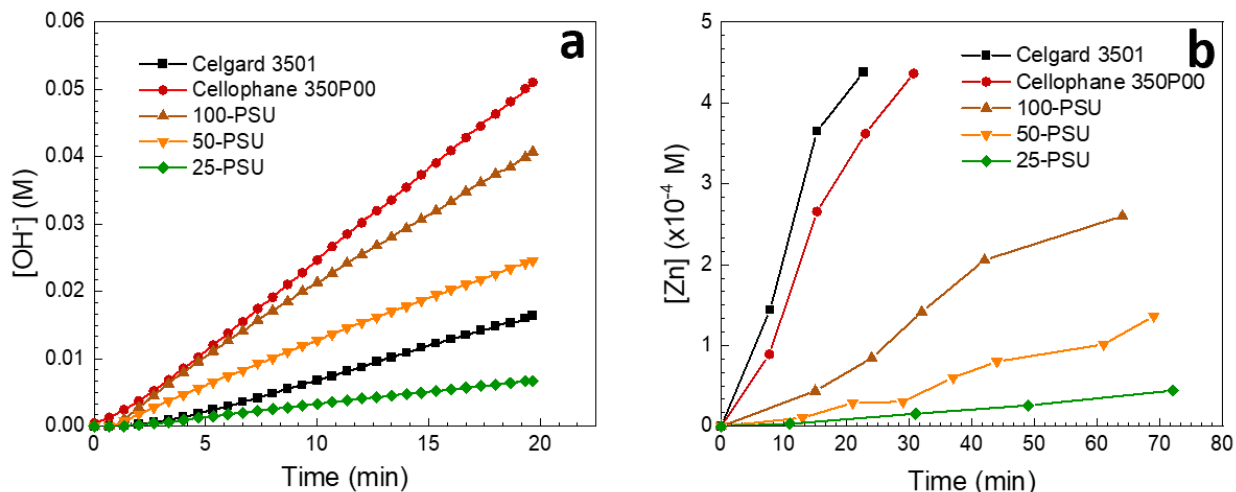
**Figure 2.** Concentration vs. time in the draw solution of the H-cell for commercial and functionalized PSU separators measuring **a)** hydroxide crossover and **b)** zincate crossover.

The rate of zincate diffusion was measured using the aforementioned diffusion cell and once again iteratively separating the draw and feed solutions with each membrane. In all cases, the rate of zincate diffusion was slower than that of hydroxide, which is likely, in general, due to the lower average diffusion velocity of larger molecules. For example, experimentally, the porous structure of Celgard affords a nonselective pathway for both large and small ions to pass through resulting in the high $D_{Zn}$ value of $5.7 \pm 0.8 * 10^{-6}$ cm$^2$ min$^{-1}$. Cellophane proved only marginally more effective at blocking zincate ions ($D_{Zn} = 2.0 \pm 0.8 * 10^{-6}$ cm$^2$ min$^{-1}$), possibly due to a size-based screening effect, as ion transport in cellophane originates from hydration-induced swelling of the polymer structure rather than discrete pores.[47] The aqueous hydroxide ion has a radius of 0.11 nm, whereas the zincate ion has a "rigid" radius of 0.30 nm and a hydrodynamic radius of 0.34 nm [in concentrated (4 M) NaOH at 25°C].[37, 48-49] The 100-PSU and 50-PSU functionalized polysulfones, on the other hand, reduced zincate crossover by an order of magnitude with $D_{Zn} = 0.42 \pm 0.02$ x$10^{-6}$ and $D_{Zn} = 0.17 \pm 0.04$ x $10^{-6}$ cm$^2$ min$^{-1}$, respectively. The 25-PSU variant showed

a two-order-of-magnitude reduction in zincate crossover rate, with $D_{Zn} = 0.049 \pm 0.002$ x $10^{-6}$ cm$^2$ min$^{-1}$ (**Table 1**, **Figure 2**).

To quantify each separator's permeability to hydroxide over zincate, a selectivity ratio, denoted as $R_s$, was calculated using equation 2.

$$R_S = \frac{D_{OH}}{D_{Zn}} \qquad (2)$$

Of the commercial separators, cellophane ($R_s = 8.5 \pm 3$) performed better than Celgard ($R_s = 1.2 \pm 0.2$), likely due to the inherently more tortuous path associated with a dense polymer structure over a porous one. The functionalized separators, which also possess a dense polymer structure, demonstrated $R_s$ values of $36 \pm 2$, $55 \pm 10$, and $51 \pm 3$ for 100-PSU, 50-PSU, and 25-PSU, all of which outperform cellophane. Besides size screening, we hypothesize that the high selectivity of our materials is explained by charge screening due to the positively charged nature of the N-butylimidazolium functional groups on the PSU backbone. Although zincate is more negatively charged (-2) than hydroxide (-1), zincate has a threefold larger ionic radius, resulting in a more diffuse charge. The functionalized polymer will therefore have a stronger electrostatic attraction to hydroxide relative to zincate. At the same time, increasing the ratio of functionalized polymer in the separator will increase overall interactions with both hydroxide and zincate, which is why 50-PSU (as opposed to 100-PSU) appears to exhibit the best selectivity.

The exact mechanism responsible for hydroxide selectivity is nearly impossible to decipher from transport studies alone and will likely require molecular modeling (currently ongoing and will be reported in a subsequent communication) to better understand the polymer structure and interactions between hydroxide and zincate with the polymer and included water. For example, if one examines going from 25-PSU to 50-PSU in Table 1: the $D_{OH}$ and $D_{Zn}$ both increase by as

13

similar factor of ~ 3.5-3.8 with a ~ 2-fold increase in water uptake. Going from 50-PSU to 100-PSU increases the $D_{OH}$ by 1.6x and the $D_{Zn}$ by 2.5x, despite the fact that the water intake again increases by roughly 2-fold. From this it is evident that the exact structure of the polymer and the density of sites is a critical factor that will require future investigation to better understand the selectivity factors that are exhibited in this class of polymers.

The separators were further characterized using electrochemical impedance spectroscopy (EIS) due to its better representation of permeability than the Gurley number in electrolyte solutions.[25] The ionic conductivity of each separator was calculated from the intercept with the real impedance axis on the Nyquist plot (**Figure 3**), along with the exposed area and thickness of each separator. Our PSU-based separators were slightly more resistive than the commercial separators, which may suggest lower permeability but is more likely a consequence of poorer wetting, consistent with the lower water uptake of our separators. Nevertheless, their ionic conductivities were still within the same order of magnitude (**Table 1**), and conductivity increased with extent of functionalization due to more electrolyte absorption. This measurement is an important performance metric for battery separators because it is expected to inform about possible rate limitations and associated voltage losses within the cell.
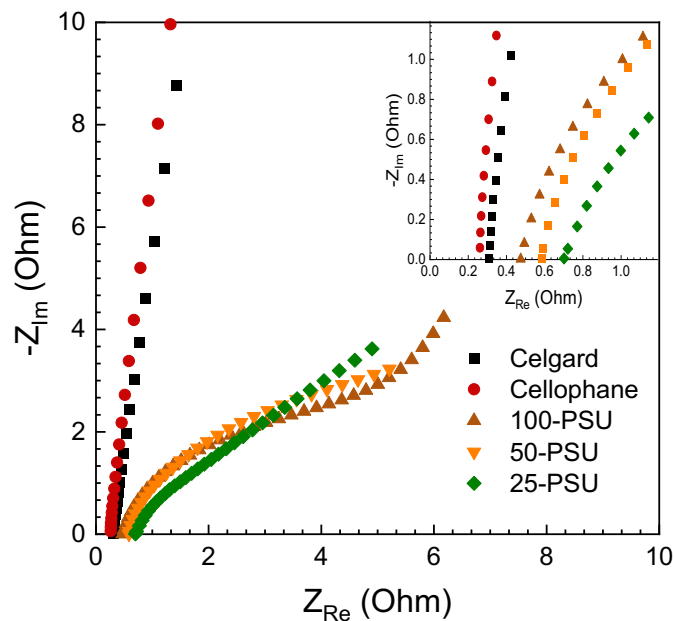
**Figure 3.** Nyquist plot of commercial and synthesized separators soaked in 4 M KOH electrolyte; AC impedance measured from 1 MHz to 1kHz.

Considering that 50-PSU showed the highest ionic selectivity of our polymers with only modest losses in conductivity compared to commercial separators, we chose to evaluate it further as a separator in a rechargeable Zn–MnO$_2$ cell containing the aforementioned Bi/Cu-modified MnO$_2$ (Bi/Cu-MnO$_2$) cathodes that were shown by Yadav et al.[5] to deliver the full two-electron capacity of MnO$_2$ reversibly. The 50-PSU membrane was inserted between the wrapped electrodes (see Experimental section for full details) and the cell was cycled at a C/10 rate (relative to the nominal cathode capacity) with voltage limits of -1 and 0.35 V vs. Hg/HgO and 100% MnO$_2$ capacity limit (equivalent to ~10% of the Zn capacity). Under the same testing conditions, the cell with the inserted 50-PSU separator significantly outlasted the PSU-free control (**Figure 4**). The latter lasted only 21 cycles until falling below 50% of the 2-electron capacity (308 mAh/g), whereas the former lasted 79 cycles until reaching the same threshold. Additionally, the cell containing PSU exhibited a slower decline in energy, staying over 70 Wh/L until the 53$^{rd}$ cycle,

whereas the control fell below this level after just 17 cycles. Furthermore, the 50-PSU-containing cell showed excellent coulombic efficiencies of over 95% until the 62$^{nd}$ cycle.
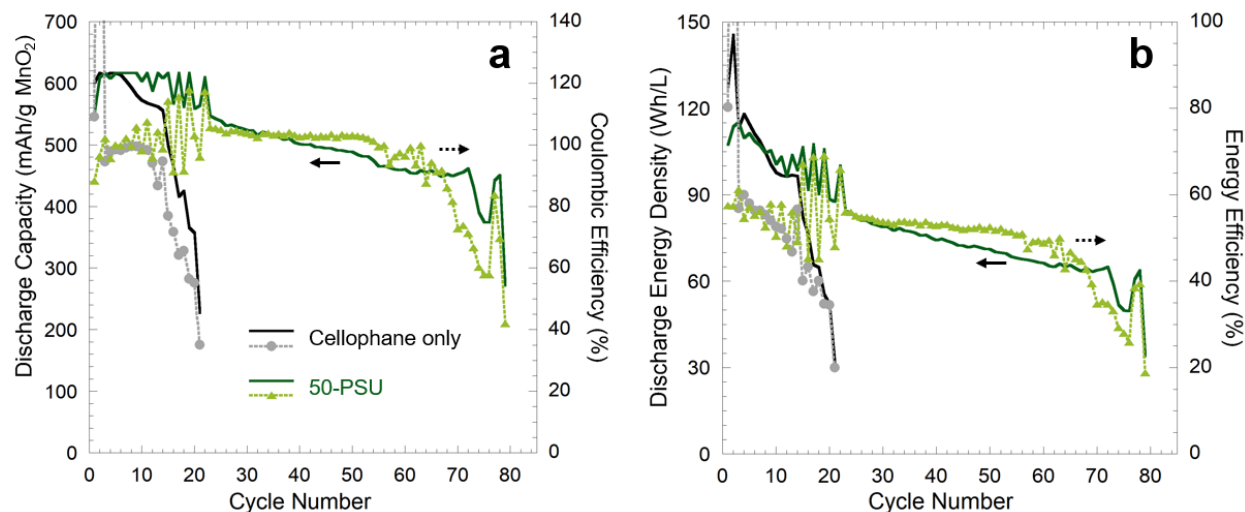


**Figure 4.** Performance of Zn/[Bi/Cu-MnO$_2$] cathode-limited cells cycled at 100% MnO$_2$ DOD and 10% Zn DOD, with a 50-PSU separator with cellophane only. **a)** Discharge capacity (solid lines) and coulombic efficiency (dashed lines). **b)** Discharge energy density (solid lines) and energy efficiency (dashed lines). Energy density was defined relative to the volume between and including the electrodes (1.22 mL).

The cathode voltage profiles during cycling provide insight into the differing performance of the cells (**Figure 5a**, **b**). In both cells after the first cycle, the highest discharge plateau, representing the Mn$^{IV}$ → Mn$^{III}$ and Mn$^{III}$ → Mn$^{II}$ transitions in δ-MnO$_2$ [birnessite, which forms *in situ* from electrolytic manganese dioxide (EMD) after the first cycle],[5, 50] is sloped rather than flat, and it loses potential, capacity, and definition over the course of cycling. Despite this loss of energy, the capacity does not decrease significantly in the first few cycles. These observations reflect the interactions of zincate with the cathode reactions, and are consistent with an earlier study showing that zincate initially reacts with the Bi/Cu-stabilized cathode to form chalcophanite (ZnMn$_3$O$_7$·3H$_2$O), a layered Zn-birnessite structure that retains some reversibility, which later

16

converts to irreversible hetaerolite $(ZnMn_2O_4)$.[16]  While the cathodes in both cells show the effects of zincate early on, we note that zincate can still diffuse around the PSU membrane (or simply go through it, as it is not completely impenetrable to zincate) and that our slow cycling rate of C/10 could allow this to happen after the first cycle.  Nevertheless, it is clear that the membrane greatly hinders zincate crossover within the battery, consistent with the transport studies above, as the Mn discharge plateau declines much more slowly in the PSU-containing cell.  By only the 10th cycle, this plateau in the control is no longer distinguishable and is around 20 mV lower than the PSU-containing cell, where the plateau does not disappear until cycle 23 under our cycling conditions.
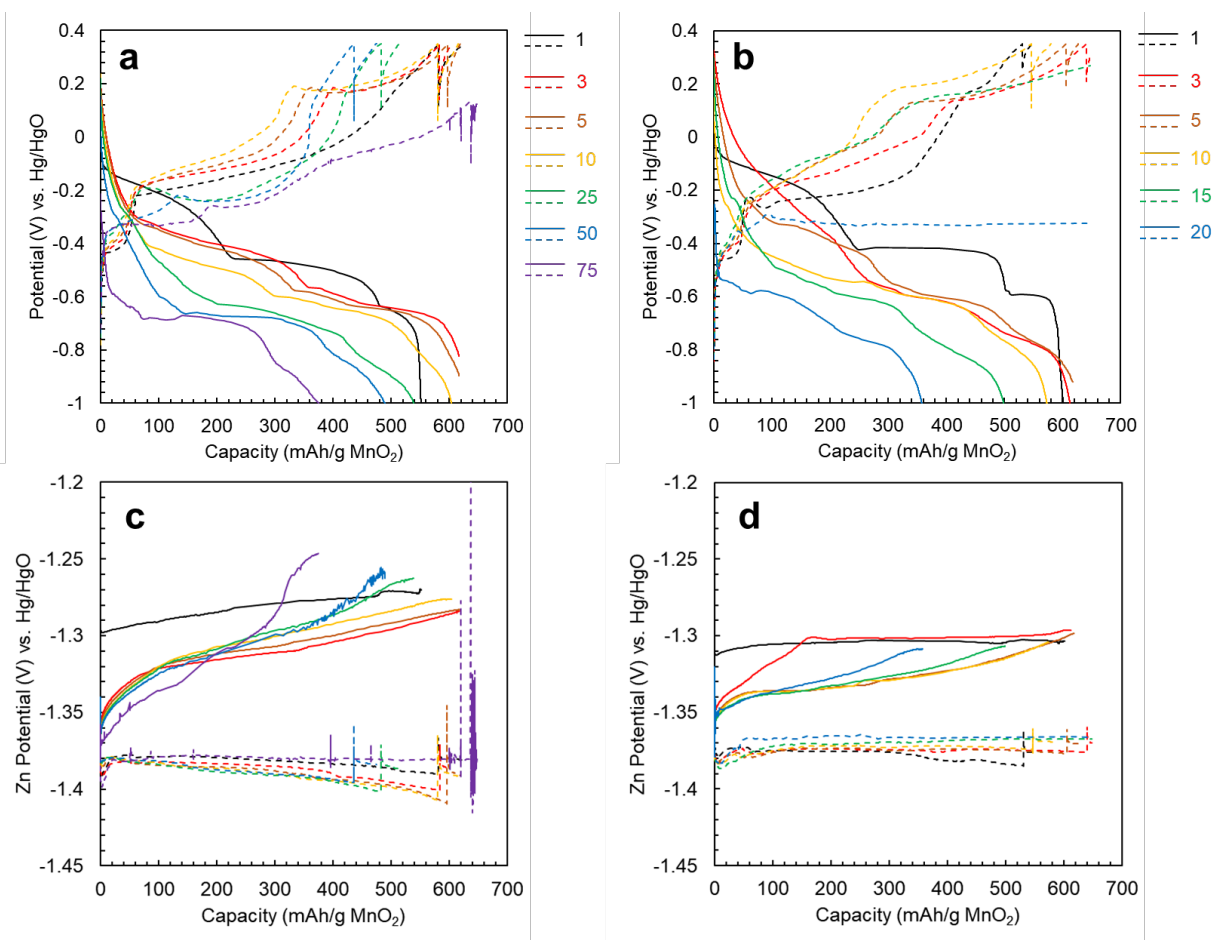
**Figure 5.** Discharge profiles (solid lines) and charge profiles (dashed lines) from selected cycles of Zn/[Bi/Cu-MnO$_2$] cells (from Figure 4) with **(a**, **c)** 50-PSU or with **(b**, **d)** cellophane only. **(a**, **b)** show cathode potential and **(c**, **d)** show anode potential versus Hg/HgO reference.

The charge voltage profiles also reflect the effect of zincate, where the features likewise become more sloped after the first cycle. Also, during cycling of the PSU cell, the major charge plateau originally between -0.2 and 0 V vs. Hg/HgO becomes depressed and flatter, while the upper plateau between 0.15 and 0.35 V vs. Hg/HgO becomes shorter and more sloped. This transition is also consistent with the earlier study of Yadav et al.[16] The first of these charge features is associated with the combination of Mn$^{II}$ $\rightarrow$ Mn$^{III}$ and Cu$^0$ $\rightarrow$ Cu$^{II}$ transitions, and the second

with the $Mn^{III} \rightarrow Mn^{IV}$ transition.[5] Since $Mn^{II} \rightarrow Mn^{III}$ occurs at a slightly lower potential than $Cu^0 \rightarrow Cu^{II}$, the depression of this plateau indicates loss of Cu electroactivity, which may be due to hetaerolite trapping and restricting further intercalation of Cu ions. At high active material loadings as used here, the loss of Cu hampers $MnO_2$ reversibility even in the absence of zincate.[50]

The transitions of the voltage profiles of the PSU cell are most abrupt between cycles 10 and 23, explaining the fluctuations in capacity and coulombic efficiency in that range (Figure S4). Here, the high-capacity charge half-cycles have profiles that are similar in character to the first 9 cycles. These are followed by high-capacity discharge half-cycles that have a shallower-sloped, longer Mn reduction region that starts above -0.4 V vs. Hg/HgO or 0.9 V vs. Zn in some cases. However, the ensuing charge-discharge sequence has lower capacities with the aforementioned depression of the main charge plateau and sloping of the upper charge plateau, whereas the discharge profile shows a more sloped, shorter Mn reduction feature whose onset is consistently below -0.4 V vs. Hg/HgO. (In this work, because we define a cycle as beginning with discharge followed by charge, the coulombic efficiencies fluctuate with the discharge capacity.) After cycle 23, the fluctuations end, the Mn reduction feature is reduced to a mere inflection point, and the charge profiles consistently show the "new" character, with little subsequent change in the nature of the charge/discharge profiles except for a gradual decline of the potentials and shortening of the initial Mn reduction slope. The period of fluctuation in capacity and voltage profiles may therefore reflect alternating formation of $\delta$-$MnO_2$ and chalcophanite on charge, before the latter is consistently formed due to the increasing concentration of zincate in the electrolyte. In addition, although this fluctuating behavior was not present in the control cells analyzed here, it has been observed in other similarly constructed cells, so we do not believe it is specifically related to the PSU membrane.

Furthermore, the voltage profiles indicate that both cells failed by shorting, where the control cell shows a much faster onset of shorting than its PSU-containing counterpart. Beginning in cycle 15, the control cell can no longer reach the voltage limit of 0.35 V vs. Hg/HgO on charge before reaching the capacity limit. Thereafter, the charge voltage continues to decline, accompanied by a steep drop in discharge capacity as Mn and Cu species can no longer fully oxidize on charge, until at cycle 20, the voltage simply levels out around -0.32 V vs. Hg/HgO on charge. Shorting was confirmed by measuring the open-circuit voltage of the cell on the final charge before disassembly, where it dropped below -1 V vs. Hg/HgO in 7.5 hours. In contrast, the 50-PSU-containing cell does not show the initial signs of shorting until cycle 72. In both cells, however, the discharge capacity is still relatively high (over 450 mAh/g) when shorting manifests, and only afterward does it fall rapidly. Thus, while the hetaerolite formation resulted in significant energy losses and gradual capacity fade due to increased resistance and effective loss of Mn, Bi, and/or Cu, shorting was the ultimate cause of cell failure. We note that this is a common failure mode of alkaline Zn–MnO$_2$ cells cycled at rates similar to ours at limited Zn utilization ($\leq$ 15%), where in those cases Zn grows through the pores of the separators and is globular rather than dendritic in morphology.[51]

Post-mortem analysis supports this mechanism of cell failure, as both cells had significant accumulation of Zn outside the anode. Interestingly, the cell with the PSU membrane had extensive Zn growth onto the bottom of the cell, whereas the control cell had no visible Zn there (**Figure S3**). However, upon disassembly, the cellophane wrapped on the anode in the 50-PSU cell was relatively clean except for the bottom edge where Zn had clearly grown through, whereas the cellophane and cellulose tissue on the anode in the control cell were completely darkened with metallic deposits (**Figure S4a**, **b**). The cathodes from both cells had extensive deposition onto

their cellophane separators as well, such that the cellophane became fused to the cathode, brittle, and difficult to peel off (**Figure S4c**, **d**). However, the PSU membrane was quite clean, was easy to peel off, and maintained its mechanical integrity (**Figure S4c**). Furthermore, while SEM imaging of the membrane on the cathode-facing side revealed numerous round crystalline deposits ($\leq 10$ μm in diameter), no obvious holes in the membrane were found, and EDS analysis showed that the deposits contained Zn, Mn, and O, suggesting that they were hetaerolite rather than metallic Zn (**Figure S5 and Figure S6**). All these observations suggest that in the control, Zn grew directly through the separators to the cathode, whereas in the PSU- containing cell, Zn grew around the bottom of the PSU separator rather than directly through it due to the screening ability of the separator. This would explain the slower failure of the PSU- containing cell despite having the same failure mechanism.

In addition, analysis of the cycled cathodes from both cells confirmed the presence of hetaerolite. XRD patterns consisted predominantly of peaks from hetaerolite, with smaller peaks corresponding to CNTs, Cu, and possibly $\lambda$-MnO$_2$ in the control cathode (**Figure 6a**). $\lambda$-MnO$_2$ is a spinel phase that has been reported to occur upon discharging and re-charging an electrode initially containing nanoscale $\beta$-MnO$_2$ in alkaline electrolyte.[52] No peaks were observed from $\gamma$-MnO$_2$ (the predominant phase of EMD) or $\delta$-MnO$_2$; however, amorphous manganese oxide and/or hydroxide may still be present.[5, 16, 50, 53] XRD of a pristine cathode showed prominent peaks of $\gamma$-MnO$_2$, akhtenskite ($\varepsilon$-MnO$_2$), Bi(OH)$_3$, and $\alpha$-Bi$_2$O$_3$ (monoclinic), the latter of which obscured the broad CNT peak. The apparent presence of hexagonal $\varepsilon$-MnO$_2$ is actually an artifact of the extensive twinning typical for EMD, which makes its crystal structure pseudo-hexagonal.[8] SEM/EDS characterization of both cycled cathodes showed that the bulk was carbon-rich, with abundant filamentous deposits (similar to the ones observed on the cycled PSU membrane) rich in

Zn, Mn, O, and Bi (**Figure S7, S8**). Interestingly, these deposits were especially concentrated within and adjacent to cracks in the electrode surface. This may occur because the sharp edges of the cracks and the effective reduction in electrode thickness generate a locally stronger electric field that attracts zincate ions more strongly during discharge. The co-location of Bi with Zn, Mn, and O suggests incorporation of Bi within the hetaerolite structure, which may have arisen from transformation of $Bi^{3+}$-intercalated chalcophanite and/or complexation of zincate with $Bi_2O_3$, which is known to occur in strongly alkaline electrolytes.[16, 54-55] The pristine cathode (**Figure S9**) also had a carbon-rich bulk, but with finer, more evenly dispersed particles, and no detectable Zn (as expected) from EDS, consistent with XRD analysis (**Figure 6**). EDS also revealed that most of these particles were rich in Mn and O, while other separate particles were rich in Bi, as expected from the cathode formulation.

XRD of the cycled anodes showed mainly Zn and ZnO with a single peak at $2\theta = 18°$ characteristic of PTFE, similar to the pristine anode material (**Figure 6b**). However, the anode from the PSU- containing cell had much more intense ZnO peaks relative to Zn peaks compared to the control and pristine anode. This is consistent with the lighter appearance of the anode from the PSU-containing cell and may be due to its longer total cycling time (66 vs. 37 days for the control) along with the screening effect of the PSU membrane, which would locally supersaturate the electrolyte above the anode with zincate and lead to accumulation of ZnO on the anode surface. Nevertheless, the average potential of the Zn anode during discharge relative to Hg/HgO did not change significantly over the course of testing for either cell except for the first 4 cycles (**Figure 5c, d**), indicating that the anode alone was not a factor in cell failure. Furthermore, the anodes did not show much shape change (redistribution of material) upon disassembly, either visibly or through sectioning of the anode and weighing of each piece (**Figure S10**). This contrasts with

similar cells cycled at the full 2-electron capacity of $MnO_2$ and 15% Zn utilization, where anodes developed large overpotentials on discharge, severe shape change, and complete conversion to ZnO, contributing to cell failure along with formation of hetaerolite in the cathode.[16]
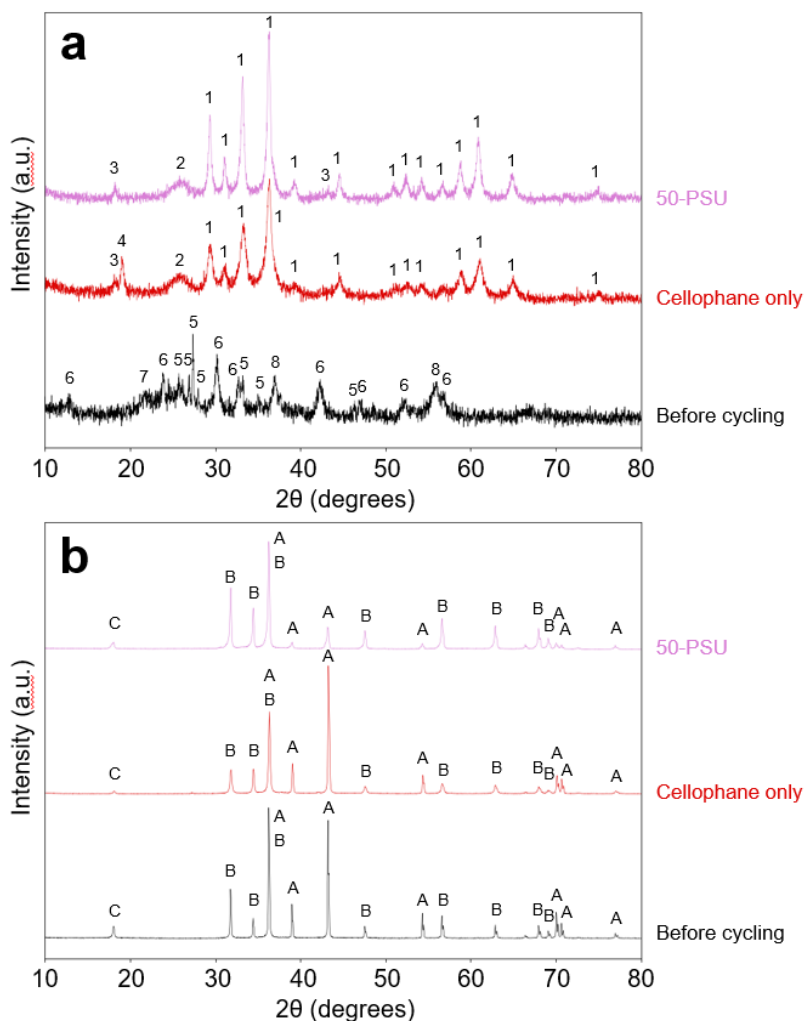


**Figure 6. a)** XRD patterns of cycled cathode with 50-PSU, cycled cathode with cellophane only, and pristine cathode. Peaks for $ZnMn_2O_4$ (1), CNT (2), Cu (3), $\lambda$-$MnO_2$ (4), $\alpha$-$Bi_2O_3$ (5), $Bi(OH)_3$ (6), $\gamma$-$MnO_2$ (7), and $\varepsilon$-$MnO_2$ (8) are shown. **b)** XRD patterns of cycled anode with 50-PSU, cycled anode with cellophane only, and pristine anode. Peaks for Zn (A), ZnO (B), and PTFE (C) are shown.

## Conclusions

In summary, a N-butylimidazolium-functionalized polysulfone was synthesized in 2 steps and blended with unmodified polysulfone (containing 25%, 50%, and 100% of functionalized PSU). Membranes cast from these blends proved to be promising zincate-blocking materials in alkaline electrolytes. Hydroxide and zincate transport screening assays show that the PSU-based separators have reduced permeability for zincate relative to commercial separators while maintaining comparable hydroxide diffusivity and overall conductivity. The separator with 50% functionalized PSU (50-PSU) exhibits the best selectivity for hydroxide over zincate, while the absolute ion diffusivities, water uptake, and conductivity all increase with the extent of functionalization.

As a proof of concept, we tested the 50-PSU membrane as a separator in rechargeable Zn–$MnO_2$ batteries with 10% Zn DOD and Bi/Cu-modified $MnO_2$ cathodes that can deliver the full two-electron capacity of $MnO_2$ (~ 100% DOD) but are sensitive to zinc crossover. The PSU-based separator extended cell lifetime from 21 to 79 cycles before falling below 50% of the two-electron capacity, and it also slowed the decline in energy density without significantly reducing it initially relative to the control cell with commercial separators. Voltage analysis during cycling and post-mortem characterization by SEM/EDS and XRD confirmed that the membrane impeded zincate diffusion and blocked growth of Zn directly across the electrodes, slowing hetaerolite formation and short-circuiting respectively, thereby improving battery cycle life and performance. These results indicate that zincate blocking separator materials could be beneficial not only for Zn–$MnO_2$ systems, but for alkaline zinc battery technologies in general, where confining zincate is necessary to prevent shape change and shorting.

## Experimental Section

**Materials.** For polymer synthesis, polysulfone (PSU, average $M_w$ ~35,000 g/mol by LS, average $M_n$ ~16,000 g/mol by MO), chloromethyl methyl ether (technical grade), chloroform (ACS reagent grade, containing 0.5-1.0% ethanol as stabilizer), and anhydrous DMF were purchased from Sigma-Aldrich. Anhydrous ethyl ether (stabilized HPLC grade), methanol (HPLC grade), and zinc chloride (USP granular) were purchased from Fisher Scientific and N-(n-butyl)imidazole was purchased from Lancaster Synthesis, Inc. All reagents and solvents were used as received from their respective manufacturers, without further purification. NMR spectra were obtained using a Bruker Avance III 500 MHz spectrometer.

For the $Cu/Bi-MnO_2$ cathodes, EMD was obtained from Tronox, $Bi_2O_3$ powder was obtained from Sigma-Aldrich, and multi-wall carbon nanotubes were obtained from CNano Technology Limited. For all Zn anodes, zinc powder was purchased from Umicore, and zinc oxide powder (99.00%, certified ACS) and sodium dodecylbenzenesulfonate (SDBS; hard type, >95.0%) were both purchased from Fisher Scientific. Sintered NiOOH anodes were purchased from Jiangsu Highstar Battery Manufacturing and used without modification. Polytetrafluoroethylene (PTFE; DISP 30, ~60 wt. % aqueous dispersion) was obtained from Chemours. Potassium hydroxide (KOH; 90%, flakes) and polyethylene glycol (PEG 400) were both purchased from Aldrich and tartaric acid (>99.0%) from Fischer Scientific. Nickel and copper mesh (4NI6-060DBFA and 5CU6-060DBFA) were purchased from Dexmet Corporation. Nickel welding strips (spooled, 6 mm width x 0.1 mm thickness) were obtained from MTI Corporation. Celgard 3501 separators were obtained from Celgard LLC, and Cellophane 350P00 separators from Innovia Films Inc.

Polyolefin nonwoven membrane (FS 2192 SG) was purchased from Freudenberg. Cellulose fiber tissue separators were purchased from Kimberly-Clark. ABS shims (1 3/8" wide, ¼" thick) and ultrahigh molecular weight polyethylene (UHMWPE) U-channels (1 ½" inside width) were purchased from McMaster-Carr. Polypropylene battery cases (Flex-A-Top, FT9, 1 ½" W x 5/8" D x 2 ½" H) were purchased from LA Container Inc. All materials and reagents were used as received, without further purification.

**Synthesis of Chloromethylated Polysulfone (CMPSU).** 1.5090 g (43.114 µmol, 35,000 g/mol avg. $M_w$, 1 equiv.) of polysulfone (PSU) were dissolved in 22.75 mL of $CHCl_3$ (1.895 mM in PSU), while stirring at 45°C – NOTE: when using commercially available beads of PSU this dissolution can take nearly an hour. 0.3735 g (2.741 mmol, 63.565 equiv.) of $ZnCl_2$ was added to this solution, followed by a slow addition of 2.735 mL (2.8991 g, 36.009 mmol, 835.20 equiv.) of chloromethyl methyl ether (CMME) in several portions. After finishing the addition of CMME the flask was filled with Ar, capped, and stirred at 45°C for 5.25 h. At this point the flask was removed from the oil bath, allowed to cool for 20 min, and the solution was precipitated from 500 mL of MeOH. After washing twice more with 150 mL of MeOH the large mass of precipitated polymer was shredded into small pieces, split between two pre-tared 50 mL centrifuge tubes, and each tube was washed sequentially with 45 mL of DI $H_2O$, 2 x 45 mL of MeOH, and 2 x 45 mL of DI $H_2O$, at which point pH paper indicated a neutral pH. A final 45 mL MeOH wash of each centrifuge tube was done to remove as much $H_2O$ as possible and the tubes were dried in a vacuum desiccator overnight to yield 1.6064 g of CMPSU. $^1H$ NMR (500 MHz, DMSO-$d_6$) $\delta$ 7.983-6.814 (br m, 15H), 4.636 (br s, 2H), 1.620 (br s, 6H). Degree of chloromethylation: 0.975 per repeat unit of PSU, based on NMR integrations.

**Synthesis of N-Butylimidazolium-functionalized Polysulfone.** 1.5865 g (40.854 µmol CMPSU, 3.231 "mmol" chloromethyl groups assuming 1 per repeat unit of PSU) of CMPSU were dissolved in 5.9 mL of anhydrous DMF (6.924 mM in CMPSU, 547.654 "mM" in chloromethyl groups assuming 1 per repeat unit of PSU), while stirring at 45°C – NOTE: similarly to dissolution of PSU in CHCl$_3$, this can take a significant amount of time. 1.540 mL (1.4630 g, 11.780 mmol, 3.646 equiv. per chloromethyl group assuming 1 chloromethyl group per repeat unit of PSU) of N-(n-butyl)imidazole were then added to the solution, the flask was filled with Ar, capped, and stirred at 45°C for 45.75 hours. At this point the flask was removed from the oil bath, allowed to cool for 2 h, and the solution was diluted with 23.5 mL of DMF. Separately, a beaker was filled with 500 mL of Et$_2$O, set to stir rapidly on a stir plate, and the entirety of the reaction solution was precipitated from this. Using 2 pre-tared centrifuge tubes, the precipitate was centrifuged, and supernatant discarded in portions, while the bulk of the precipitated polymer was kept covered and rapidly stirring – NOTE: without the stirring the precipitate showed a tendency to reabsorb DMF from the supernatant. Finally, the centrifuge tubes were dried in a vacuum desiccator to yield a hard semisolid that retained an appreciable amount of solvent and was difficult to break up. ^{1}H NMR (500 MHz, DMSO-$d_6$) $\delta$ 9.505 and 9.300 (two separate s, totaling 1H, depending on attachment position of N-butylimidazolium), 7.987-6.889 (m, 17H), 5.456 and 5.416 (two separate s, totaling 2H, depending on attachment position of N-butylimidazolium), 4.030 (m, 2H), 1.684 (t, 6H), 1.598 (m, 2H), 1.109 (m, 2H), 0.805 (m, 3H). Degree of functionalization: 0.975 per repeat unit of PSU, based on NMR integrations from the previous chloromethylation step.

**Separator Fabrication.** N-butylamidizolium functionalized polysulfone and unfunctionalized polysulfone were dissolved in DMF to 5 wt. % concentrations. Solutions for the 25-PSU and 50-PSU separators were made by combining functionalized and unfunctionalized solutions in the

proper proportions (measured by volume) in a glass scintillation vial. 3 mL of solution was pipetted into a 7.5 x 3.5 cm casting tray that was made in-house from an ultra-high molecular weight polyethylene (UHMWPE) U-channel (McMaster-Carr). The separators were then dried in an oven at 75°C for 4 hours. Deionized water was used to float the finished separators off the tray surface.

**Water Uptake Measurements.** To measure water uptake, separators were placed in deionized water for 24 h. The separators were then removed from the water, patted dry with an absorbent cloth to remove excess water drops from the surface, and weighed. The separators were then dried for 24 h in a vacuum oven at 60°C and weighed again. The water uptake percentage for each separator was calculated using the following equation:

$$Water\ Uptake\ (\%) = \frac{m_w - m_d}{m_d}\ X\ 100$$

where $m_w$ is the mass of the separator after soaking in deionized water and $m_d$ is the mass of the separator after drying in the vacuum oven.

**Ionic Conductivity Measurements.** Potentiostatic electrochemical impedance spectroscopy (PEIS) was used to measure the through-plane ionic conductivities of the separators. The impedance measurements were carried out on a Gamry Interface 5000E bipotentiostat. Separators were cut into 3/8" diameter circles and soaked in 4 M KOH overnight before being placed in a Swagelok cell with stainless steel blocking electrodes on either side, built similarly to the cell used by Hudak et al.[56] A frequency range of 1 MHz to 1 kHz was used with a sinusoidal amplitude of 5 mV from open-circuit potential at room temperature. The resistance of the separator was determined by finding the x-intercept on the Nyquist plot, where the imaginary impedance is zero. Ionic conductivity was calculated using the equation:

$$\sigma = \frac{\tau}{R_b A}$$

where $\tau$ is the thickness of the separator, $R_b$ is the bulk resistance obtained from the Nyquist plot, and $A$ is the cross-sectional area (0.7123 cm$^2$).

**Hydroxide Diffusion Measurements.** Hydroxide diffusion was measured using a high-density polyethylene two-chamber diffusion cell and an Orion VersaStar Pro pH meter. The feed side of the diffusion cell contained 8.5 M KOH while the draw side contained deionized water. The pH of the draw solution was sampled every 5 sec and a diffusion coefficient was calculated using the following equation:

$$D_{OH} = \frac{V_D \tau}{At} \ln \left( \frac{C_F}{C_F - C_D} \right)$$

where $D_{OH}$ is the diffusion coefficient for hydroxide, $V_D$ is the volume of the draw solution (30 mL), $\tau$ is the thickness of the separator (25 μm for Celgard and Cellophane, 30 μm for the polymeric separators), $A$ is the exposed cross sectional area of the separator (1.17 cm$^2$), $C_F$ is the concentration of hydroxide in the feed solution (8.5 M), and $C_D$ is the concentration of hydroxide in the draw solution measured over time. Each test was run for at least 20 min and the reported diffusion coefficient is an average of the calculated diffusion coefficient for each data point in the 20 min testing period.

**Zincate Diffusion Measurements.** Anodic stripping voltammetry (ASV) was used to measure the rate of zincate diffusion across the separators following the method from Duay, et al.[30] Electrochemical testing was performed using a Pine WaveDriver 20 potentiostat. The working electrode was a 3 mm glassy carbon disc electrode from BASi. The counter and reference

electrodes were a graphite rod and a Hg/HgO electrode (1 M KOH), respectively. Testing was done in the presence of dissolved oxygen.

Separators were placed in the same two-chamber diffusion cells used for hydroxide diffusion testing. The draw solution consisted of 8.5 M KOH with 2.5 ppm Pb, 2.5 ppm Cd, and 5 ppm Bi. The feed solution was 4 wt. % ZnO in 8.5 M KOH with 2.5 ppm Pb, 2.5 ppm Cd, and 5 ppm Bi. A 30 s cleaning step at 0.3 V under stirring was followed by a deposition step at -1.75 V, also under stirring. Stirring was then stopped, and a 25 s rest step was carried out while applying a -1.75 V potential. Square wave voltammetry was performed from -1.75 V to 0.3 V with a 5 mV amplitude, 25 mV pulse, and 0.05 s duration resulting in a scan rate of 100 mV s$^{-1}$.

ASV measurements were done periodically on the draw solution to measure zincate concentration over a period of minutes or hours, as necessary. A zincate diffusion coefficient, $D_{Zn}$, was calculated for each data point using the previously shown equation, where $C_F$ was the concentration of zinc in the feed solution and $C_D$ was the concentration of zinc in the draw solution.

**Battery Construction and Testing.** Cycling tests with and without the 50-PSU separator were performed with Bi/Cu-modified MnO$_2$ cathodes paired with Zn anodes. As shown previously by Yadav et al.,[5, 16] these cathodes are designed for reversible cycling at the full two-electron capacity of MnO$_2$ (617 mAh g$^{-1}$), which is not possible with conventional EMD electrodes. The cathodes for this study were built similarly to these earlier reports. Briefly, 55 wt. % EMD, 10 wt. % Bi$_2$O$_3$, and 35 wt. % CNTs were ball-milled and then made into a slurry by adding water. Copper was added as a metal compressed against the cathode mix at an area loading of 0.016 g/cm$^2$, rather than being intermixed with the other cathode components. ~0.5 g of mix was pasted onto a 1 x 1 in. nickel mesh, dried, and pressed at 10 tons. The finished cathode was sealed in one layer of

polyolefin nonwoven membrane (FS 2192 SG, Freudenberg), then wrapped in 3 layers of cellophane.

Zinc anodes were made as described in our previous work,[13, 44, 57] mixing 83.1 wt. % Zn powder, 9.8 wt. % ZnO powder, 2.2 wt. % SDBS, and 4.9 wt. % PTFE solids in a mortar and pestle and adding isopropanol to produce a malleable putty. Individual anodes were cut as 1 x 1 in. pieces from the putty, with their mass tailored such that the theoretical two-electron capacity of the Bi/Cu-$MnO_2$ cathode ($\approx$ 170 mAh) was approximately 10% of the theoretical anode capacity. Each anode was then dried at 60°C and pressed at 1500 psi onto a copper mesh current collector of the same size with an adjoining tab cut from the same piece of mesh. Each anode was then wrapped in 3 layers of cellophane followed by 4 layers of cellulose tissue.

The 50-PSU membrane was cut to a 1.25 x 1.25 in. square and was pre-soaked for at least 48 h in 25 wt. % KOH electrolyte. It was then inserted between the fully wrapped electrodes, and the entire assembly was placed in a cell case with one ABS shim (1 1/16" wide, ¼" thick) and 4 mL of 25 wt. % KOH electrolyte. After soaking overnight, an identical shim was added to fully compress the electrodes, 1.4 mL electrolyte was added (to make a total volume of 5.4 mL), and a Hg/HgO reference electrode (Pine Research, RREF0038) was inserted into the cell case.

Galvanostatic cycling was performed on an Arbin LBT21084 multi-channel battery tester. Cells were assembled in the charged state, so cycling began with discharge at a rate of C/10 (relative to the theoretical 2-electron capacity of the cathode $\approx$ 170 mAh) until either the full 2-electron capacity was discharged or the cathode potential reached -1 V vs. Hg/HgO. Following a 2 min rest step, charging proceeded at C/10 until reaching 105% of the 2-electron capacity or a cathode potential of 0.35 V vs. Hg/HgO. If the voltage limit was reached before the capacity limit, the cell was rested for 30 min, then charged again at C/20 until reaching either of the

aforementioned limits.  The cell was then rested for 2 min and discharged at C/10 as previously described.  However, if the capacity limit was reached on the C/10 charge, the C/20 charging step was bypassed.  Cycling continued in this manner until failure, when the cells were charged once more as previously described and then immediately disassembled for post-mortem analysis.

Considering that our cells were assembled in the charged state, we define each cycle as starting with discharge, followed by charge. We define coulombic efficiency for each cycle as that cycle's discharge capacity divided by its charge capacity, and since discharge occurs first, it is reasonable for the coulombic efficiency to exceed 100%.

Volumetric energy density of the cells was defined relative to the volume between and including the electrodes (1.22 mL), which is a standard approach used in previous literature.[5, 14, 16, 58]  This consists of one cathode (average thickness of 0.747 mm including current collector), one layer of polyolefin nonwoven membrane on the cathode (0.125 mm thick), 6 layers of cellophane (3 on the cathode, 3 on the anode at 0.025 mm per layer), 4 layers of cellulose tissue on the anode (0.025 mm per layer), and one anode (average thickness of 0.890 mm including current collector), for a total thickness of 1.89 mm. Multiplying this by the cross-sectional area of 1" x 1" (645 mm$^2$) gives a volume of 1.22 mL.

**Post-Mortem Analysis**

The cycled electrodes and separators were rinsed and soaked in deionized water for at least 3 d to remove as much residual KOH as possible, then dried at rt.  For X-ray diffraction (XRD), the cycled anodes were cut to fit in a sample holder (1" diameter) and placed face-up; the anode material was not removed from the current collector.  For the cycled cathodes, a portion was removed from the current collector and ground to a powder before placing in the XRD sample holder, since the lack of electrode binder caused the material to break apart upon drying anyway.

Scans were performed on a Bruker D2 Phaser X-ray diffractometer with Cu Kα radiation ($\lambda_{K\alpha}$ = 1.54 Å), from 2θ = 10–80° with step size 0.02°, step time 0.5 s and rotating the sample 6 times per min. Spectra were analyzed with Bruker DIFFRAC.SUITE EVA software and the International Centre for Diffraction Data (ICDD) database.

Scanning electron microscopy (SEM) and energy-dispersive X-ray spectroscopy (EDS) were performed on the cathodes and functionalized PSU membrane before and after cycling, using a field-emission Zeiss GeminiSEM 500 at 5 kV or 20 kV accelerating voltage and 9.5–11.2 mm working distance. For the cathodes, a piece of the dried material was removed from the current collector and placed on conductive carbon tape on an aluminum sample stub, such that the outward-facing surface of the cathode material was up. The membranes were mounted similarly, but required sputter-coating with Au/Pd prior to analysis to minimize charging. For the cycled membrane, a small piece was cut from the center and mounted with the cathode-facing side up.

## Author Information

**Corresponding Author**
* E-mail: tnlambe@sandia.gov

## Supporting Information

Supporting information contains polymer characterization spectra, additional cycling data, as well as post-mortem photos and analysis.

## References

1.      ARPA-E, *GRIDS Program Overview*. U.S. Department of Energy: Washington, D.C., 2010.

2.      Marsal, P. A.; Kordesch, K.; Urry, L. F. DRY CELL. 2,960,558, 1960.

3.      Gallaway, J. W.; Erdonmez, C. K.; Zhong, Z.; Croft, M.; Sviridov, L. A.; Sholklapper, T. Z.; Turney, D. E.; Banerjee, S.; Steingart, D. A., Real-Time Materials Evolution Visualized within Intact Cycling Alkaline Batteries. *Journal of Materials Chemistry A* **2014,** *2* (8), 2757-2764.

4.      Hertzberg, B. J.; Huang, A.; Hsieh, A.; Chamoun, M.; Davies, G.; Seo, J. K.; Zhong, Z.; Croft, M.; Erdonmez, C.; Meng, Y. S.; Steingart, D., Effect of Multiple Cation Electrolyte Mixtures on Rechargeable Zn–MnO2 Alkaline Battery. *Chemistry of Materials* **2016,** *28* (13), 4536-4545.

5.      Yadav, G. G.; Gallaway, J. W.; Turney, D. E.; Nyce, M.; Huang, J.; Wei, X.; Banerjee, S., Regenerable Cu-Intercalated MnO2 Layered Cathode for Highly Cyclable Energy Dense Batteries. *Nature Communications* **2017,** *8*, 14424.

6.      United States Environmental Protection Agency, Standards for Universal Waste Management. 2019; Vol. 40 CFR Part 273.

7.      Dzieciuch, M. A.; Gupta, N.; Wroblowa, H. S., Rechargeable Cells with Modified MnO2 Cathodes. *Journal of The Electrochemical Society* **1988,** *135* (10), 2415-2418.

8.      Gallaway, J. W.; Hertzberg, B. J.; Zhong, Z.; Croft, M.; Turney, D. E.; Yadav, G. G.; Steingart, D. A.; Erdonmez, C. K.; Banerjee, S., Operando Identification of the Point of [Mn2]O4 Spinel Formation During γ-MnO2 Discharge within Batteries. *Journal of Power Sources* **2016,** *321*, 135-142.

9.      Gallaway, J. W.; Menard, M.; Hertzberg, B.; Zhong, Z.; Croft, M.; Sviridov, L. A.; Turney, D. E.; Banerjee, S.; Steingart, D. A.; Erdonmez, C. K., Hetaerolite Profiles in Alkaline Batteries Measured by High Energy EDXRD. *Journal of The Electrochemical Society* **2015,** *162* (1), A162-A168.

10.     McBreen, J., Zinc Electrode Shape Change in Secondary Cells. *Journal of The Electrochemical Society* **1972,** *119* (12), 1620-1628.

11.     Poa, S.-P.; Wu, C. H., The Current Distribution and Shape Change of Zinc Electrodes in Secondary Silver-Zinc Cells. *Journal of Applied Electrochemistry* **1978,** *8* (6), 491-501.

12.     Poa, S.-P.; Wu, C. H., A Quantitative Study of Shape Change in Zinc Secondary Electrodes. *Journal of Applied Electrochemistry* **1978,** *8* (5), 427-436.

13.     Lim, M. B.; Lambert, T. N.; Ruiz, E. I., Effect of ZnO-Saturated Electrolyte on Rechargeable Alkaline Zinc Batteries at Increased Depth-of-Discharge. *Journal of The Electrochemical Society* **2020,** *167* (6), 060508.

14.     Ingale, N. D.; Gallaway, J. W.; Nyce, M.; Couzis, A.; Banerjee, S., Rechargeability and Economic Aspects of Alkaline Zinc–Manganese Dioxide Cells for Electrical Storage and Load Leveling. *Journal of Power Sources* **2015,** *276*, 7-18.

15.     Banerjee, S., Progress on the Development of the Zn-MnO2 Rechargeable Battery. In *U.S. Department of Energy Office of Electricity Peer Review*, Albuquerque, NM, 2019.

16.     Yadav, G. G.; Wei, X.; Huang, J.; Gallaway, J. W.; Turney, D. E.; Nyce, M.; Secor, J.; Banerjee, S., A Conversion-Based Highly Energy Dense Cu2+ Intercalated Bi-Birnessite/Zn Alkaline Battery. *Journal of Materials Chemistry A* **2017,** *5* (30), 15845-15854.

17.     Zhang, S. S., A Review on the Separators of Liquid Electrolyte Li-Ion Batteries. *J. Power Sources* **2007,** *164* (1), 351-364.

18.     Huang, X., Separator Technologies for Lithium-Ion Batteries. *J. Solid State Electrochem.* **2011,** *15* (4), 649-662.

19.     Weber, C. J.; Geiger, S.; Falusi, S.; Roth, M., Material Review of Li Ion Battery Separators. *AIP Conf. Proc.* **2014,** *1597* (1, Review on Electrochemical Storage Materials and Technology), 66-81.

20.     Lee, H.; Yanilmaz, M.; Toprakci, O.; Fu, K.; Zhang, X., A Review of Recent Developments in Membrane Separators for Rechargeable Lithium-Ion Batteries. *Energy Environ. Sci.* **2014,** *7* (12), 3857-3886.

21.     Banerjee, A.; Ziv, B.; Shilina, Y.; Ziegelbauer, J. M.; Liu, H.; Harris, K. J.; Botton, G.; Goward, G. R.; Luski, S.; Aurbach, D.; Halalay, I. C., Review-Multifunctional Separators: Durability and Performance of Li-Ion Batteries. *J. Electrochem. Soc.* **2019,** *166* (3), A5369-A5377.

22.     Lagadec, M. F.; Zahn, R.; Wood, V., Characterization and Performance Evaluation of Lithium-Ion Battery Separators. *Nat. Energy* **2019,** *4* (1), 16-25.

23.     Hsu, L. C.; Sheibley, D. W., Inexpensive Crosslinked Polymeric Separators Made from Water-Soluble Polymers. *J. Electrochem. Soc.* **1982,** *129* (2), 251-254.

24.     Sheibley, D. W.; Manzo, M. A.; Gonzalez-Sanabria, O. D., Crosslinked Poly(Vinyl Alcohol) Films as Alkaline Battery Separators. *J. Electrochem. Soc.* **1983,** *130* (2), 255-259.

25.     Arora, P.; Zhang, Z., Battery Separators. *Chem. Rev.* **2004,** *104* (10), 4419-4462.

26.     Lee, J.-S.; Kim, S. T.; Cao, R.; Choi, N.-S.; Liu, M.; Lee, K. T.; Cho, J., Metal-Air Batteries with High Energy Density: Li-Air Versus Zn-Air. *Adv. Energy Mater.* **2011,** *1* (1), 34-50.

27.     Li, Y.; Dai, H., Recent Advances in Zinc-Air Batteries. *Chem. Soc. Rev.* **2014,** *43* (15), 5257-5275.

28.     Gu, P.; Zheng, M.; Zhao, Q.; Xiao, X.; Xue, H.; Pang, H., Rechargeable Zinc-Air Batteries: A Promising Way to Green Energy. *J. Mater. Chem. A* **2017,** *5* (17), 7651-7666.

29.     McLarnon, F. R.; Cairns, E. J., The Secondary Alkaline Zinc Electrode. *Journal of The Electrochemical Society* **1991,** *138* (2), 645-656.

30.     Duay, J.; Lambert, T. N.; Aidun, R., Stripping Voltammetry for the Real Time Determination of Zinc Membrane Diffusion Coefficients in High pH: Towards Rapid Screening of Alkaline Battery Separators. *Electroanalysis* **2017,** *29* (10), 2261-2267.

31.     Huang, J.; Yadav, G. G.; Gallaway, J. W.; Wei, X.; Nyce, M.; Banerjee, S., A Calcium Hydroxide Interlayer as a Selective Separator for Rechargeable Alkaline Zn/MnO2 Batteries. *Electrochem. Commun.* **2017,** *81*, 136-140.

32.     Dewi, E. L.; Oyaizu, K.; Nishide, H.; Tsuchida, E., Cationic Polysulfonium Membrane as Separator in Zinc-Air Cell. *J. Power Sources* **2003,** *115* (1), 149-152.

33.     Miyazaki, K.; Lee, Y. S.; Fukutsuka, T.; Abe, T., Suppression of Dendrite Formation of Zinc Electrodes by the Modification of Anion-Exchange Ionomer. *Electrochemistry* **2012,** *80* (10), 725-727.

34.     Stock, D.; Dongmo, S.; Miyazaki, K.; Abe, T.; Janek, J.; Schröder, D., Towards Zinc-Oxygen Batteries with Enhanced Cycling Stability: The Benefit of Anion-Exchange Ionomer for Zinc Sponge Anodes. *Journal of Power Sources* **2018,** *395*, 195-204.

35.     Stock, D.; Dongmo, S.; Walther, F.; Sann, J.; Janek, J.; Schröder, D., Homogeneous Coating with an Anion-Exchange Ionomer Improves the Cycling Stability of Secondary Batteries with Zinc Anodes. *ACS Applied Materials & Interfaces* **2018,** *10* (10), 8640-8648.

36.     Stock, D.; Dongmo, S.; Damtew, D.; Stumpp, M.; Konovalova, A.; Henkensmeier, D.; Schlettwein, D.; Schröder, D., Design Strategy for Zinc Anodes with Enhanced Utilization and Retention: Electrodeposited Zinc Oxide on Carbon Mesh Protected by Ionomeric Layers. *ACS Applied Energy Materials* **2018,** *1* (10), 5579-5588.

37.     Wu, Y.; Zhang, Y.; Ma, Y.; Howe, J. D.; Yang, H.; Chen, P.; Aluri, S.; Liu, N., Ion-Sieving Carbon Nanoshells for Deeply Rechargeable Zn-Based Aqueous Batteries. *Advanced Energy Materials* **2018,** *8* (36), 1802470.

38.     Zhang, Y.; Wu, Y.; Ding, H.; Yan, Y.; Zhou, Z.; Ding, Y.; Liu, N., Sealing ZnO Nanorods for Deeply Rechargeable High-Energy Aqueous Battery Anodes. *Nano Energy* **2018,** *53*, 666-674.

39.     Wu, G. M.; Lin, S. J.; You, J. H.; Yang, C. C., Study of High-Anionic Conducting Sulfonated Microporous Membranes for Zinc-Air Electrochemical Cells. *Mater. Chem. Phys.* **2008,** *112* (3), 798-804.

40.     Huang, J.; Yadav, G. G.; Turney, D.; Nyce, M.; Banerjee, S., A Permselective Graphene Oxide/Polyvinyl Alcohol Composite Membrane for Rechargeable Alkaline Zinc Manganese Dioxide Batteries. *ECS Meeting Abstracts* **2018**.

41.     Huang, J.; Yadav, G. G.; Nyce, M.; Banerjee, S. Ion Selective Membrane for Selective Ion Penetration in Alkaline Batteries. WO2019046575A1, 2019.

42.     Lee, H.-J.; Lim, J.-M.; Kim, H.-W.; Jeong, S.-H.; Eom, S.-W.; Hong, Young T.; Lee, S.-Y., Electrospun Polyetherimide Nanofiber Mat-Reinforced, Permselective Polyvinyl Alcohol

Composite Separator Membranes: A Membrane-Driven Step Closer toward Rechargeable Zinc–Air Batteries. *Journal of Membrane Science* **2016,** *499*, 526-537.

43.      Kim, H.-W.; Lim, J.-M.; Lee, H.-J.; Eom, S.-W.; Hong, Y. T.; Lee, S.-Y., Artificially Engineered, Bicontinuous Anion-Conducting/-Repelling Polymeric Phases as a Selective Ion Transport Channel for Rechargeable Zinc-Air Battery Separator Membranes. *J. Mater. Chem. A* **2016,** *4* (10), 3711-3720.

44.      Duay, J.; Kelly, M.; Lambert, T. N., Evaluation of a Ceramic Separator for Use in Rechargeable Alkaline Zn/MnO2 Batteries. *J. Power Sources* **2018,** *395*, 430-438.

45.      Cellophane PØØ Data. In *Ref A220*, Futamura Group.

46.      Celgard High Performance Battery Separators. In *Literature Item 10002*, Celgard: 2009.

47.      Pavai, M.; Szabo, T.; Paszternak, A., The Potential Use of Cellophane Test Strips for the Quick Determination of Food Colours. *Cellulose (Dordrecht, Neth.)* **2015,** *22* (3), 1883-1891.

48.      Marcus, Y., Volumes of Aqueous Hydrogen and Hydroxide Ions at 0 to 200 °C. *The Journal of Chemical Physics* **2012,** *137* (15), 154501.

49.      Pessine, E. J.; Agostinho, S. M. L.; Chagas, H. C., Evaluation of the Diffusion Coefficient of the Zincate Ion Using a Rotating Disk Electrode. *Canadian Journal of Chemistry* **1986,** *64* (3), 523-527.

50.      Yadav, G. G.; Wei, X.; Gallaway, J. W.; Chaudhry, Z.; Shin, A.; Huang, J.; Yakobov, R.; Nyce, M.; Vanderklaauw, N.; Banerjee, S., Rapid Electrochemical Synthesis of δ-MnO2 from γ-MnO2 and Unleashing Its Performance as an Energy Dense Electrode. *Materials Today Energy* **2017,** *6*, 198-210.

51.      Turney, D. E.; Gallaway, J. W.; Yadav, G. G.; Ramirez, R.; Nyce, M.; Banerjee, S.; Chen-Wiegart, Y.-c. K.; Wang, J.; D'Ambrose, M. J.; Kolhekar, S.; Huang, J.; Wei, X., Rechargeable Zinc Alkaline Anodes for Long-Cycle Energy Storage. *Chemistry of Materials* **2017,** *29* (11), 4819-4832.

52.      Seo, J. K.; Shin, J.; Chung, H.; Meng, P. Y.; Wang, X.; Meng, Y. S., Intercalation and Conversion Reactions of Nanosized β-MnO2 Cathode in the Secondary Zn/MnO2 Alkaline Battery. *The Journal of Physical Chemistry C* **2018,** *122* (21), 11177-11185.

53.      Gallaway, J. W.; Yadav, G. G.; Turney, D. E.; Nyce, M.; Huang, J.; Chen-Wiegart, Y.-c. K.; Williams, G.; Thieme, J.; Okasinski, J. S.; Wei, X.; Banerjee, S., An Operando Study of the Initial Discharge of Bi and Bi/Cu Modified MnO2. *Journal of The Electrochemical Society* **2018,** *165* (13), A2935-A2947.

54.      Renuka, R.; Ramamurthy, S.; Srinivasan, L., Interaction of Zincate with Additives Turbidimetric, IR and Raman Spectral Analyses. *Journal of Power Sources* **2000,** *89* (1), 70-79.

55.      Renuka, R.; Srinivasan, L.; Ramamurthy, S.; Veluchamy, A.; Venkatakrishnan, N., Cyclic Voltammetric Study of Zinc and Zinc Oxide Electrodes in 5.3 M KOH. *Journal of Applied Electrochemistry* **2001,** *31* (6), 655-661.

56.      Hudak, N. S.; Small, L. J.; Pratt, H. D.; Anderson, T. M., Through-Plane Conductivities of Membranes for Nonaqueous Redox Flow Batteries. *Journal of The Electrochemical Society* **2015,** *162* (10), A2188-A2194.

57.      Kelly, M.; Duay, J.; Lambert, T. N.; Aidun, R., Impact of Triethanolamine as an Additive for Rechargeable Alkaline Zn/MnO2 Batteries under Limited Depth of Discharge Conditions. *Journal of The Electrochemical Society* **2017,** *164* (14), A3684-A3691.

58.      Duay, J.; Lambert, T. N.; Kelly, M.; Pineda-Dominguez, I., Rechargeable Solid-State Copper Sulfide Cathodes for Alkaline Batteries: Importance of the Copper Valence State. *Journal of The Electrochemical Society* **2019,** *166* (4), A687-A694.

**TOC Graphic**